

# Wall-bounded thermal turbulent convection driven by heat-releasing point particles

Yuhang Du<sup>1,2</sup> and Yantao Yang<sup>1,2,†</sup>

<sup>1</sup>State Key Laboratory for Turbulence and Complex Systems, and Department of Mechanics and Engineering Science, College of Engineering, Peking University, Beijing 100871, PR China

<sup>2</sup>Joint Laboratory of Marine Hydrodynamics and Ocean Engineering, Pilot National Laboratory for Marine Science and Technology (Qingdao), Shandong 266299, PR China

(Received 18 July 2022; revised 21 November 2022; accepted 22 November 2022)

In this work we investigate the thermal convection driven by heat-releasing point particles. Three-dimensional direct numerical simulations are conducted for  $1 \times 10^7 \leq Ra \leq 1 \times 10^{10}$  and  $0.01 \leq St \leq 10$ , where the Rayleigh number  $Ra$  and Stokes number  $St$  measure the strengths of the heat releasing rate and the Stokes drag, respectively. A regime at intermediate Stokes numbers is identified with most particles accumulating into the top boundary layer region, while for other cases particles are constantly advected over the entire domain. For the latter state, the flow motions are stronger at the upper part of the domain. The thicknesses of both momentum and thermal boundary layers at the top plate follow the same scaling law with  $Ra$  and show minor dependences on  $St$ . The volume-averaged temperature and convective flux exhibit non-monotonic variations as  $St$  increases and reach their minimums at intermediate  $St$ . The fraction coefficient of heat flux, i.e. the ratio between the heat flux through the bottom plate and the total flux through both plates, shares the similar dependence on  $St$  as the convective flux. The relation between these scaling laws can be explained by using the global balance between the dissipation and convective flux. The scaling laws for the transition between different flow regimes are also proposed and agree with the numerical results. The preferential concentration of particles is observed for all cases and is strongest at intermediate Stokes numbers, for which multiscale clustering emerges with small clusters forming larger ones.

**Key words:** particle/fluid flow, turbulent convection

## 1. Introduction

The particle-laden thermal flows are commonly encountered in various natural and engineering applications. Astrophysical and geophysical examples include the interaction

† Email address for correspondence: [yantao.yang@pku.edu.cn](mailto:yantao.yang@pku.edu.cn)

between the cloud and radiation (Shaw 2003), and aggregation of chondrules into primitive planetesimals (Cuzzi *et al.* 2001). For engineering processes, the particle-based solar receivers are designed to directly absorb solar energy by small particles in the work fluid (Pouransari & Mani 2017). In all these environments, particles can strongly affect the flow dynamics compared with the single-phase thermal convection. Numerous studies have been conducted to understand the coupling mechanisms between particles and turbulence.

For a fluid layer with dilute particles, i.e. the volume fraction of solid particles is small compared with the total mixture volume, the interaction between particles can be ignored (Crowe 1982; Elghobashi 1994; Balachandar & Eaton 2010). Then the coupling mechanisms introduced by particles are the momentum coupling and thermal coupling between the fluid carrier phase and the dispersed particle phase. Many studies have been conducted by considering the thermal and momentum interactions between particles and turbulent flows. Shotorban, Mashayek & Pandya (2003) investigated such a problem for homogeneous shear turbulence with the temperature field driven by constant background gradient, and found out that the turbulent heat flux decreases after introducing the particle phase. For turbulent particle-laden channel flow with thermal and momentum coupling, Kuerten, van der Geld & Geurts (2011) also observed that the turbulent heat flux decreases with the presence of particles. However, much more heat is transported by relative motion of particles, which results in a net enhancement of heat transfer compared with the single-phase channel flow without particles.

In the above-mentioned works, the temperature field is treated as a passive scalar, which is, the temperature field is advected by the velocity field but the momentum dynamics is not affected by the temperature field. In reality the fluid density often depends on temperature and buoyancy-driven convection occurs in the gravity field. A suitable model system for such a problem is the particle-laden Rayleigh–Bénard convection (RBC), i.e. convection flow between two horizontal plates across which an unstable temperature difference is applied. Oresta & Prosperetti (2013) studied the modulation of RBC caused by particle settling. The particles have constant temperature which does not change as the particles move. The momentum coupling, thermal coupling and the combined coupling are considered for their effects on the heat flux. Besides the thermal and momentum coupling between the particle and fluid, Park, O’Keefe & Richter (2018) also included the thermal dynamics of particles in the model. The behaviours of both heat flux and turbulent kinetic energy were investigated with varying particle inertia, settling velocity, mass fraction and the ratio of specific heat. In the recent work of Yang *et al.* (2021), only the momentum coupling between two phases was considered. The temperature of particles is constant and affects the particle dynamics through the thermophoresis effect. When the momentum coupling is strong, both the heat transfer and turbulent kinetic energy are greatly enhanced.

The present study focuses on another mechanism of the particle-laden buoyancy-driven flow. That is, particles can obtain energy from some external sources such as radiation, and then release the energy into the fluid phase. With this process the particles not only modify the momentum and thermal dynamics of the fluid phase through particle–fluid coupling, but also serve as a driving mechanism. Such externally heated particles have been studied for several groups for incompressible and compressible homogeneous turbulence in a fully periodic domain (Zamansky *et al.* 2014, 2016; Frankel *et al.* 2016; Pouransari & Mani 2017). The RBC with externally heated particles was investigated very recently by Pan *et al.* (2022), in which two-way momentum and thermal couplings were also considered. The convection flow is then driven together by the temperature difference between the top and bottom boundary and by the heating source from particles. Here we are interested in the convection flow driven purely by the heating effects of particles which absorb energy

from external supplies. Meanwhile, the one-way coupling of momentum and two-way coupling of temperature are included between particles and the fluid phase.

It should be pointed out that our configuration is similar to certain extent to the radiatively driven RBC. Several experimental works have been conducted recently for such a system. Special dye can be used to absorb the external light radiation and which releases heat into fluid which drives the convection motions (Lepot, Aumaitre & Gallet 2018; Bouillaut *et al.* 2019; Creyssels 2020). These experiments reveal that the scaling law of heat flux is very different from the RBC driven by the external temperature difference. Experiments on radiation-absorbing particles in turbulent duct flow reveal the fluid temperature rising and different preferential concentration behaviours at the core region and near the boundary (Banko *et al.* 2020).

The current work can also be viewed as the extension of our previous works on the RBC driven by a heat-releasing concentration field (Du, Zhang & Yang 2021, 2022), where the concentration field releases heat at a constant rate and is advected by the convection motions. Here, we conduct a systematic study on the RBC driven by point particles which absorb energy from external sources and drive the convection motion by heating up the surrounding fluid. Particle distributions and global fluxes will be discussed and a theoretical model will be developed based on the Grossmann–Lohse (GL) theory for RBC (Grossmann & Lohse 2000, 2001, 2002, 2004).

The rest of paper is organized as follows. In § 2 we describe the governing equation and numerical method. Sections 3 and 4 present our numerical results and discussions about the flow regime and statistics. Finally, we give conclusions in § 5.

## 2. Governing equations and numerical methods

### 2.1. Governing equations and key parameters

Consider a fluid layer bounded by two horizontal plates which are separated by a height  $H$  and are perpendicular to gravity. Dispersed solid particles are carried by the fluid phase. The fluid density is assumed to be linearly dependent on temperature as  $\rho = \rho_0(1 - \alpha\theta)$ . Here,  $\rho_0$  is the density at the reference state,  $\theta = T - T_0$  is the temperature deviation with respect to the value at the reference state and  $\alpha$  is the thermal expansion coefficient, respectively. In the current study we set the top and bottom plates at the same constant temperature  $T_0$ , saying the value of the reference state. By using the Oberbeck–Boussinesq approximation, the governing equations for the fluid phase read

$$\nabla^* \cdot \mathbf{u}^* = 0, \tag{2.1a}$$

$$\partial_t^* \mathbf{u}^* + \mathbf{u}^* \cdot \nabla^* \mathbf{u}^* = -\nabla^* p^* + \nu \nabla^{*2} \mathbf{u}^* + g\alpha\theta^* \mathbf{e}_z + \mathbf{f}^*, \tag{2.1b}$$

$$\partial_t^* \theta^* + \mathbf{u}^* \cdot \nabla^* \theta^* = \kappa \nabla^{*2} \theta^* + q^*. \tag{2.1c}$$

Here,  $\mathbf{u} = (u, v, w)$  is the fluid velocity vector,  $p$  is pressure,  $\nu$  is kinematic viscosity,  $g$  is gravitational acceleration. The extra source term  $\mathbf{f}$  in (2.1b) represents the rate of momentum exchange with point particles. The rate of heat exchange between fluid and particles is denoted by  $q$  in (2.1c). The asterisk superscript stands for the dimensional quantities or operators.

The dispersed particles are treated by the Lagrangian framework, which is, the dynamic and thermal equations are solved simultaneously as the particles are tracked. The particle size is assumed to be smaller than the Kolmogorov scale so that they can be viewed as

zero-volume points. The full set of particle equations used in the current study read

$$\frac{d\mathbf{x}_p^*}{dt^*} = \mathbf{u}_p^*, \tag{2.2a}$$

$$\frac{d\mathbf{u}_p^*}{dt^*} = \frac{\mathbf{u}_f^* - \mathbf{u}_p^*}{\tau_p} - g \left( 1 - \frac{\rho_0}{\rho_p} \right) \mathbf{e}_z, \tag{2.2b}$$

$$\frac{d\theta_p^*}{dt^*} = \frac{\theta_f^* - \theta_p^*}{\tau_\theta} + \frac{\phi_p^*}{m_p c_p}. \tag{2.2c}$$

Hereafter, the subscript ‘*p*’ denotes the quantity related to the particle, and ‘*f*’ is the fluid quantity at the same location of particle, respectively. As can be seen from (2.2*b*), the acceleration of particles is caused by the Stokes drag and buoyancy force. The Stokes time is defined as  $\tau_p = \rho_p d_p^2 / \rho_0 18\nu$  with  $d_p$  being the particle diameter. The two terms in the right-hand side of (2.2*c*) stand for the heat exchange with surrounding fluid and the heating rate caused by an external input such as radiation. The former is approximated by the relaxation of the particle temperature towards the fluid temperature with the time scale  $\tau_\theta = (3/2)(\nu/\kappa)(c_p/c_f)\tau_p$  (Zamansky *et al.* 2016). Here  $c_p$  and  $c_f$  are the heat capacities of the solid particle and fluid. In the second term,  $\phi_p$  is the power of external energy input into a single particle and  $m_p$  is the mass of particle.

The source terms in (2.1*b*) and (2.1*c*) can be calculated by the Stokes drag in (2.2*b*) and the thermal relaxation term in (2.2*c*). In the Eulerian framework for the fluid phase, these source terms can be expressed by the Dirac distribution  $\delta(\mathbf{x})$  and the velocity and temperature differences at the locations of particle as

$$\mathbf{f}^* = \frac{\mathbf{F}^*(\mathbf{x}^*)}{\rho_0} = -\frac{1}{\rho_0} \sum_p^{N_p} m_p \frac{\mathbf{u}_f^* - \mathbf{u}_p^*}{\tau_p} \delta(\mathbf{x}^* - \mathbf{x}_p^*), \tag{2.3a}$$

$$q^* = \frac{Q^*(\mathbf{x}^*)}{\rho_0 c_f} = -\frac{1}{\rho_0 c_f} \sum_p^{N_p} m_p c_p \frac{\theta_f^* - \theta_p^*}{\tau_\theta} \delta(\mathbf{x}^* - \mathbf{x}_p^*). \tag{2.3b}$$

Here the two source terms  $\mathbf{F}^*(\mathbf{x}^*)$  and  $Q^*(\mathbf{x}^*)$  are per unit fluid volume, and the summation is over all particles.

To non-dimensionalize the governing equations, we first discuss the choice of characteristic scales for each quantity. The length scale can use the domain height  $H$  as in usual Rayleigh–Bénard (RB) flow. In RB flow, usually the free-fall velocity  $U_{ff} = \sqrt{g\alpha\Delta_T H}$  is used as the characteristic scale, with  $\Delta_T$  being the temperature difference between the bottom and top boundaries. Here the two boundaries are at the same constant temperature, therefore another temperature scale has to be used. For this we turn to the external energy input of particles. We denote the particle number density by  $n_p$ . For unit volume the total power of external energy input is  $n_p\phi_p$ , which causes a changing rate of fluid temperature at  $(n_p\phi_p)/(c_f\rho_0)$ . Then by equating this changing rate to that given by the characteristic scales for temperature, velocity and length as

$$\frac{n_p\phi_p}{c_f\rho_0} = \frac{\Delta_T\sqrt{g\alpha\Delta_T H}}{H}, \tag{2.4}$$

the temperature scale can be obtained as  $\Delta_T = (n_p^2\phi_p^2 H/g\alpha\rho_0^2 c_f^2)^{1/3}$ . The corresponding free-fall velocity is then  $U_{ff} = (g\alpha n_p\phi_p H^2/\rho_0 c_f)^{1/3}$ , and the time scale is  $\tau_f = H/U_{ff}$ .

Using these characteristic scales, the non-dimensional governing equations can be readily obtained as

$$\nabla \cdot \mathbf{u} = 0, \tag{2.5a}$$

$$\partial_t \mathbf{u} + \mathbf{u} \cdot \nabla \mathbf{u} = -\nabla p + Ra^{-1/3} Pr^{2/3} \nabla^2 \mathbf{u} + \theta \mathbf{e}_z + \mathbf{f}, \tag{2.5b}$$

$$\partial_t \theta + \mathbf{u} \cdot \nabla \theta = Ra^{-1/3} Pr^{-1/3} \nabla^2 \theta + q, \tag{2.5c}$$

$$d_t \mathbf{x}_p = \mathbf{u}_p, \tag{2.5d}$$

$$d_t \mathbf{u}_p = \frac{\mathbf{u}_f - \mathbf{u}_p}{St} - \frac{\mathbf{e}_z}{Fr^2}, \tag{2.5e}$$

$$\Phi_\theta d_t \theta_p = \frac{\theta_f - \theta_p}{\sigma} + 1, \tag{2.5f}$$

with

$$\mathbf{f} = - \sum_p^{N_p} \frac{\alpha_V \rho_p}{C \rho_0} \frac{\mathbf{u}_f - \mathbf{u}_p}{St} \delta(\mathbf{x} - \mathbf{x}_p), \tag{2.6}$$

$$q = - \sum_p^{N_p} \frac{\alpha_V \rho_p c_p}{C \rho_0 c_f} \frac{\theta_f - \theta_p}{\sigma \Phi_\theta} \delta(\mathbf{x} - \mathbf{x}_p). \tag{2.7}$$

The boundary conditions for the fluid phase at two plates are, in their non-dimensional form,

$$\mathbf{u} = \mathbf{0}, \quad \theta = 0, \quad \text{at } z = 0, \tag{2.8a}$$

$$\mathbf{u} = \mathbf{0}, \quad \theta = 0, \quad \text{at } z = 1. \tag{2.8b}$$

In the horizontal directions we employ the periodic boundary conditions for all the flow quantities and particles.

For the particle–boundary interaction, we assume elastic reflection at the upper and bottom plates and the particle temperature is unchanged during reflection, which is different from the numerical treatment in some RBC with heated particles (e.g. Yang *et al.* 2021; Pan *et al.* 2022). In those works, a particle is removed from the domain when it reaches the bottom plate. Meanwhile, a new particle is randomly ejected into the domain from a random location of the upper wall, and its temperature is equal to the local fluid temperature. In our configuration, since the heat released by particles is the sole driving force, we keep the total number of particles, and therefore the total energy input unchanged.

Key control parameters then include the Prandtl number  $Pr$ , the Rayleigh number  $Ra$ , the Froude number  $Fr$ , the Stokes number  $St$ , the heat-mixing parameter  $\sigma$ , the heat-capacity ratio  $\Phi_\theta$  and the non-dimensional particle number density  $C$ , which are defined, respectively, as

$$\left. \begin{aligned} Pr &= \frac{\nu}{\kappa}, & Ra &= \frac{g \alpha n_p \phi_p H^5}{\nu \kappa^2 \rho_0 c_f}, & Fr &= (Ra Pr)^{1/3} \left( \frac{\kappa^2}{g (1 - \rho_0 / \rho_p) H^3} \right)^{1/2}, \\ St &= \frac{\tau_p}{\tau_f}, & \sigma &= \frac{\tau_\theta}{\tau_f \Phi_\theta}, & \Phi_\theta &= \frac{n_p m_p c_p}{c_f \rho_0}, & C &= n_p H^3. \end{aligned} \right\} \tag{2.9}$$

Here,  $\Phi_\theta$  is the ratio between the total heat capacity of dispersed phase and that of fluid phase,  $C$  is the average number of particles in a volume  $H^3$ . The Froude number  $Fr$  is the

ratio of particle gravitation acceleration to the buoyancy-induced fluid acceleration. The Stokes number  $St$  is the ratio of the particle relaxation time  $\tau_p$  to the characteristic time  $\tau_f$  of flow. The heat mixing parameter  $\sigma$  is defined as the ratio of the fluid thermal relaxation time  $\tau_{\theta f} = \tau_{\theta}/\Phi_{\theta}$  to  $\tau_f$  (Pouransari & Mani 2017). Note that we selected the fluid thermal relaxation time  $\tau_{\theta f}$ , instead of the commonly used particle thermal relaxation time  $\tau_{\theta}$  to form the dimensionless heat-mixing parameter.

It can be noticed that the definition of Rayleigh number is different from that in the RBC, where the temperature difference between the two plates is usually employed. In the current system, the two plates have the same temperature and a different temperature scale has to be used. Note that for unit volume the total power input is  $n_p\phi_p$ , corresponding to a time changing rate in fluid temperature of  $\gamma = (n_p\phi_p)/(c_f\rho_0)$ . Then the Rayleigh number can be cast into  $Ra = (g\alpha\gamma H^5)/(v\kappa^2)$ , which is in the same form as that in the convection flow driven by a uniform internal heat source (Roberts 1967).

From these parameters, the volume fraction of particles, the density and heat capacity ratios between two phases can be calculated as

$$\alpha_V = \frac{Ra Pr}{48\pi^2 C^2 \sigma^3}, \quad \frac{\rho_p}{\rho_0} = \frac{72\pi^2 St C^2 \sigma^2}{Ra}, \quad \frac{c_p}{c_f} = \frac{2\sigma \Phi_{\theta}}{3St Pr}. \quad (2.10a-c)$$

Note that if all other parameters are fixed,  $\alpha_V \sim Ra$ . Therefore, for large enough  $Ra$ ,  $\alpha_V$  will also be large and four-way coupling needs to be considered.

Global responses of interests are the mean temperature  $\langle\theta\rangle_V$  of fluid, with  $\langle\cdot\rangle_V$  being the average over the flow domain and time. Note that at a statistically steady state, the total heat flux transported out of the domain through the two plates is balanced by the energy input into the particles, which is a control parameter in the current model. Therefore, it is the division of the total heat flux between the top and bottom plates that has practical importance. Similar to the internally heated RB (Goluskin & van der Poel 2016), a fraction coefficient is defined as

$$F_B = \frac{\langle\partial_z\theta\rangle_{bot}}{\langle\partial_z\theta\rangle_{bot} - \langle\partial_z\theta\rangle_{top}}, \quad (2.11)$$

with  $\langle\cdot\rangle_{top}$  and  $\langle\cdot\rangle_{bot}$  standing for the average over time and top and bottom plates, respectively. The strength of the flow motion is measured by the Reynolds number as

$$Re = \frac{U_{rms}H}{\nu}, \quad (2.12)$$

where  $U_{rms}$  is the root mean square (r.m.s.) value of the velocity magnitude.

## 2.2. Numerical methods and the explored parameter space

As discussed in the previous subsection, the parameter space is huge since seven independent control parameters need to be considered. To keep the current study manageable, we will fix  $\Phi_{\theta}$ ,  $\sigma$ ,  $C$  and  $Pr$ , and focus on the influences of  $Ra$  and  $St$ . Furthermore, two assumptions are employed to simplify the governing equations. The first one is that the particle suspension is dilute with the global volume fraction  $\alpha_V$  smaller or around  $10^{-3}$ . According to the relation (2.10a-c), this sets an upper bound for  $Ra$  with fixed  $Pr$ ,  $C$  and  $\sigma$ . As suggested in Balachandar & Eaton (2010), for such low volume fraction the one-way or two-way coupling can still be used. Therefore, we retain the particle-heating source term  $q$  in (2.5c) and set the particle-momentum source term  $\mathbf{f} = \mathbf{0}$  in (2.5b). Another assumption is that the gravitational settling term in (2.5e) is negligible

compared with the Stokes drag term, which requires  $Fr^2 \gg St$ . Note that the definition of the Froude number can be rewritten as

$$Fr = (48\pi^2)^{-5/12} \Phi_\theta^{-5/12} \sigma^{-5/4} C^{-1/12} Pr^{3/4} \left( \frac{g^3 \alpha^9 \rho_p^5 c_p^5}{\nu^9 \kappa^6 \rho_0^{14} c_f^{14}} \right)^{1/12} \phi_p^{3/4}. \quad (2.13)$$

Then for given fluid and particle material,  $Fr \sim \phi_p^{3/4}$  when  $\Phi_\theta$ ,  $\sigma$  and  $C$  are fixed. For large enough  $\phi_p$  indeed the gravitational settling effect can be neglected. With the above two assumptions, the final version of the employed governing equations reads

$$\nabla \cdot \mathbf{u} = 0, \quad (2.14a)$$

$$\partial_t \mathbf{u} + \mathbf{u} \cdot \nabla \mathbf{u} = -\nabla p + Ra^{-1/3} Pr^{2/3} \nabla^2 \mathbf{u} + \theta \mathbf{e}_z, \quad (2.14b)$$

$$\partial_t \theta + \mathbf{u} \cdot \nabla \theta = Ra^{-1/3} Pr^{-1/3} \nabla^2 \theta + q, \quad (2.14c)$$

$$d_t \mathbf{x}_p = \mathbf{u}_p, \quad (2.14d)$$

$$d_t \mathbf{u}_p = \frac{\mathbf{u}_f - \mathbf{u}_p}{St}, \quad (2.14e)$$

$$\Phi_\theta d_t \theta_p = \frac{\theta_f - \theta_p}{\sigma} + 1. \quad (2.14f)$$

Initially the particles are randomly seeded over the flow domain with a homogeneous distribution, and the temperature and velocity equal to the value of fluid at the same location. With such settings for particles, the heating source for fluid phase can be treated approximately with uniform strength at the initial time. Then a conductive solution can be solved and used as the initial velocity and temperature field, namely,

$$\mathbf{u} = \mathbf{0}, \quad \theta(z) = -Ra^{1/3} Pr^{1/3} \left( \frac{z^2}{2} - \frac{z}{2} \right), \quad (2.15)$$

in which we assume  $q = 1$  at the initial time.

The governing equations (2.14a)–(2.14c) are then discretized by using a second-order finite-difference scheme with the fractional-time-step method (Verzicco & Orlandi 1996; Ostilla-Monico *et al.* 2015). For time integration a second-order Runge–Kutta scheme is employed with the treatment of nonlinear terms similar to the Adams–Bashforth method and that of diffusion terms to the Crank–Nicholson method, respectively. The location, velocity and temperature of point particles are integrated by a second-order Runge–Kutta scheme, i.e. with the same order of accuracy as the numerical scheme for fluid phase. To obtain the quantities at the exact locations of particles, the cubic Hermite spline is used to interpolate from the Eulerian grids to the particle locations. The source terms in the momentum and temperature equations are smoothed by distributing towards the eight neighbouring Eulerian grids around each particle (Kuersten *et al.* 2011). To ensure a proper resolution in our direct numerical simulations, the mesh size is chosen to be smaller than both the Kolmogorov scale  $\eta_u = (\nu^3/\epsilon_u)^{1/4}$  and the Batchelor scale  $\eta_\theta = \eta_u Pr^{-1/2}$ . Here  $\epsilon_u = \langle \nu(\nabla \mathbf{u})^2 \rangle_V$  is the global mean dissipation rate of kinetic energy. For the convergence of each case, we check the  $F_B$  and  $Re$  averaged over the first half and second half of the time period over which the statistics are sampled and the relative different is smaller than 3%.

In the present study, the Prandtl number is fixed at  $Pr = 0.7$  corresponding to heat in air, the particle density number is fixed at  $C = 10^5$  and the two thermal parameters are set

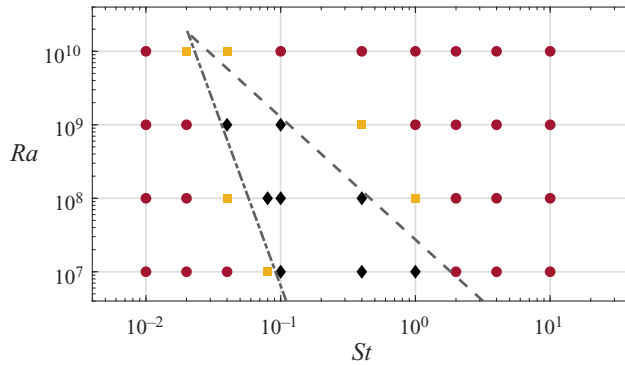


Figure 1. The explored phase space in the  $St$ - $Ra$  plane. The black diamonds mark the cases in which all the particles gradually accumulate near the top plates and simulation cannot continue. All other cases can reach a statistically steady state. For those marked by orange squares the normalized number density of particles exceeds 10 in the upper viscous boundary layer (BL), while for those marked by red circles are not. The grey dashed line marks the scaling of  $St_{cr}''$  with slope  $-5/3$ , and the grey dash-dotted line for  $St_{cr}'$  with slope  $-5$ .

as  $\Phi_\theta = 0.1$  and  $\sigma = 1$ , respectively. With these four parameters fixed, we simulated four Rayleigh numbers ranging between  $10^7$  and  $10^{10}$ , which give a maximal volume fraction around  $1.4 \times 10^{-3}$ . For each  $Ra$ , the Stokes number  $St$  is gradually increased from 0.01 to 10. The explored parameter space is shown in figure 1. Details of numerical settings and key responses are summarized in table 1 in Appendix A. Starting from the conductive state (2.15), three different final states are obtained in our simulations for different parameters, as indicated by different symbols in figure 1. For the Stokes numbers small or large enough, as marked by red circles, the flow can reach a statistically steady state with particles being convected constantly over the entire domain. For certain intermediate Stokes numbers, see the black diamonds, most particles will eventually accumulate near the top plate, leading to an extremely strong local heating source. The time step has to be reduced for the simulation to continue and finally becomes unfeasibly small. Between these two regimes, as indicated by yellow squares, the simulations can continue but the local number density near the top plate is over 10 times bigger than the global mean value. Therefore, for the cases marked by yellow squares and black diamonds, the local number density adjacent to the top plate is too high and it may be problematic in using one-way and two-way coupling in momentum and thermal interaction. However, for the cases marked by red circles, the simulation results and the physical models used are consistent with each other. The physical mechanism for the appearance of different regimes and the regime boundaries will be discussed in §4.1, and all the mean statistics will only be discussed for the cases which reach the statistically state, namely those marked by red circles in figure 1.

To give some idea about the correspondence between the non-dimensional parameters and the real physical properties, we present some examples of flow settings. With air as the carrier fluid, we take the reference density  $\rho_0 = 1.29 \text{ kg m}^{-3}$ , the kinematic viscosity  $\nu = 1.4 \times 10^{-5} \text{ m}^2 \text{ s}^{-1}$ , the thermal diffusivity  $\kappa = 2 \times 10^{-5} \text{ m}^2 \text{ s}^{-1}$ , the thermal expansion coefficient  $\alpha = 3.67 \times 10^{-3} \text{ K}^{-1}$  and the heat capacities  $c_f = 1000 \text{ J (kg K)}^{-1}$ , respectively. For silicon carbide particles the density and heat-capacity ratios are  $\rho_p/\rho_0 \approx 2469$  and  $c_p/c_f \approx 1.15$  (Jiang *et al.* 2019), one obtains  $Ra \approx 2.38 \times 10^8$  and  $St \approx 0.08$ . If copper particles are used with  $\rho_p/\rho_0 \approx 6892$  and  $c_p/c_f \approx 0.37$  (Van Heerden, Nobel & Van Krevelen 1953), one has  $Ra \approx 2.88 \times 10^8$  and  $St \approx 0.3$ . These



two sets of parameters lie in the phase space explored here. From these values one can determine the ratio between the particle diameter and domain height  $d_p/H$  around  $9 \times 10^{-4}$ , which is similar to those reported in Dritselis & Vlachos (2011).

### 3. Mean statistics and transport properties

In this section we focus on the cases in which the flow reaches a statistically steady state and particles are convected over the entire domain. These include all the cases marked by the red circles in figure 1.

#### 3.1. Global balance for statistically steady flows

When the flow is in the statistically steady state, two relations about the global balance can be obtained. At such a state, the mean temperature averaged over all particles and time should be independent of time. Then from (2.14f) one has

$$\sigma = \langle \theta_p - \theta_f \rangle_p. \quad (3.1)$$

Here  $\langle \cdot \rangle_p$  stands for the average over all particles and time. This relation suggests that the mean temperature difference between particles and the surrounding fluid is controlled by  $\sigma$ . In the current study  $\sigma$  is fixed at unity. We then compute the quantity  $\langle \theta_p - \theta_f \rangle_p$  for all the cases with a statistically steady state, which are listed in table 1 in Appendix A. The global balance is indeed achieved.

The relation (3.1) also implies that, by taking the average of (2.7),

$$\langle q \rangle_V = 1. \quad (3.2)$$

Then the spatial and temporal average of (2.14b) gives

$$Nu = Ra^{-1/3} Pr^{-1/3} \left( \left. \frac{d\langle \theta \rangle_h}{dz} \right|_{bot} - \left. \frac{d\langle \theta \rangle_h}{dz} \right|_{top} \right) = 1. \quad (3.3)$$

That is, the total non-dimensional heat flux  $Nu$  through the top and bottom plates is equal to unity once the flow is in the statistically steady state. In our simulations, the error in  $Nu$  is less than 3%, as can be seen from table 1 in Appendix A. The accuracy of these two global balance relations indicate that our numerical settings are adequate.

#### 3.2. Mean statistics of the fluid phase

We then look at the mean statistics of the carrier phase. Figure 2 shows the mean profiles for velocity and temperature fields for all the cases with  $Ra = 10^{10}$ . The profiles for r.m.s. values of the vertical velocity  $w$  and the horizontal velocity  $u_h$  indicate that the flow motions are stronger in the upper half-domain. For all Stokes numbers  $w_{rms}$  reaches the maximal value in the range  $0.6 < z/H < 0.8$ . For  $u_{hrms}$  profiles, the peaks near the top boundary are both higher and closer to the wall than those near the bottom boundary. The profiles of horizontally averaged temperature indicate the flow consists of a nearly homogeneous bulk between two BLs which both have strong temperature gradients. The profiles of the standard deviation of temperature also exhibit two strong peaks located in the top and bottom BLs.

Figure 2 reveals that the mean profiles exhibit very non-trivial variations as  $St$  increases from 0.01 to 10. Therefore, in order to obtain consistent results, we use the following

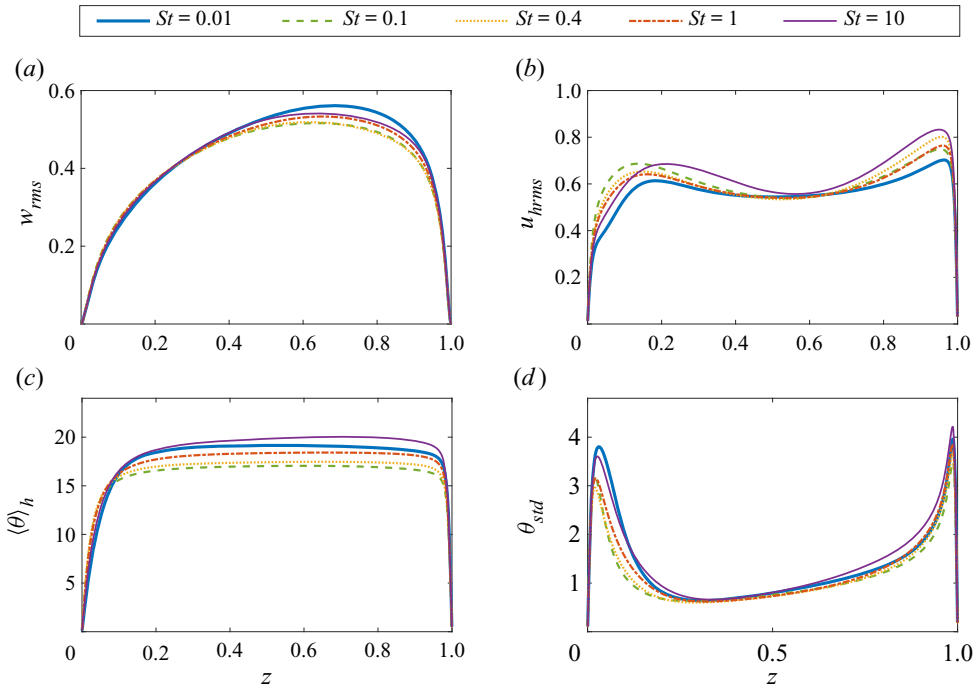


Figure 2. Mean profiles for the cases with  $Ra = 10^{10}$  and different  $St$ . (a) The r.m.s. of vertical velocity. (b) The r.m.s. of horizontal velocity. (c) The horizontally averaged temperature. (d) The standard deviation of temperature ( $\theta_{std}$ ).

definitions for the momentum and thermal BL thicknesses. Based on the r.m.s. profiles for the horizontal velocity, as shown in figure 2(b), the thicknesses of viscous BLs are extracted separately at the top and bottom plates by using the same method as in Sun, Cheung & Xia (2008). The edge of the viscous BL is determined by the intersection between the straight line which is tangential to the r.m.s. profile at the boundary and the horizontal line which is tangential to the same profile at the corresponding peak. The viscous BL thicknesses are denoted by  $\lambda_{u,top}$  and  $\lambda_{u,bot}$  for the top and bottom boundaries, respectively. The thermal BL thicknesses at the top and bottom plates are extracted from figure 2(c) as the height of the intersection between the straight line which is tangential to the mean profile at the boundary and the horizontal line with the value of volume-averaged temperature. They are denoted by  $\lambda_{\theta,top}$  and  $\lambda_{\theta,bot}$ . Similar to the RBC with uniform internal heating (Goluskin & van der Poel 2016; Wang, Lohse & Shishkina 2020), a single thermal BL thickness can be defined as  $\lambda_{\theta} = 2/(\lambda_{\theta,top}^{-1} + \lambda_{\theta,bot}^{-1})$ .

Figure 3 displays the variation of viscous BL thickness versus the Rayleigh number for different Stokes numbers. The thickness of top BL  $\lambda_{u,top}$  is only slightly affected by  $St$  and exhibits a single power-law scaling of  $Ra$ . The scaling exponent is determined by the linear fitting of data in the logarithmic scale. Note that for intermediate Stokes number, not all Rayleigh numbers correspond to cases with a statistically steady state. Therefore, the standard linear fitting is conducted for the two groups of cases with  $St = 0.01$  and 10, respectively. Then the scaling exponent is taken as the mean of two values from the fitting of two groups. Throughout the present study, the same procedure is adopted when a scaling exponent is determined for the dependence on  $Ra$ . The linear fitting suggests that

Wall-bounded turbulent driven by heat-releasing particle

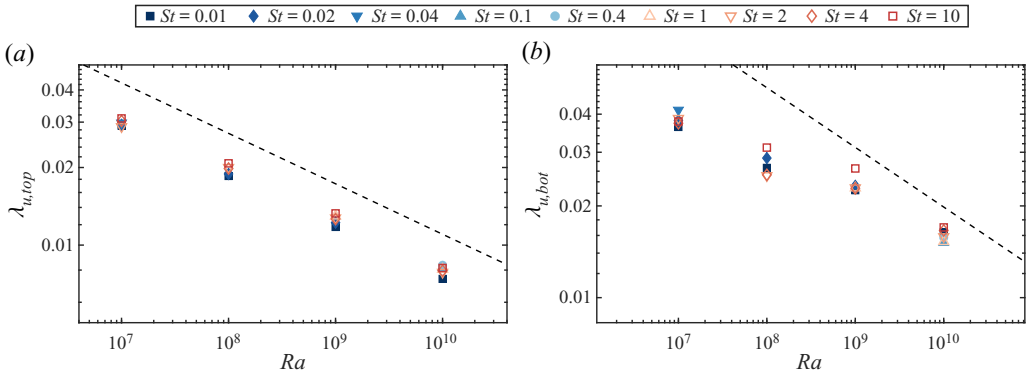


Figure 3. The thickness of (a) top viscous BL, (b) bottom viscous BL. The dashed lines in both panels have the same slope of  $-0.196$ . The value of the slope is obtained through linear regression with the details given in the main text.

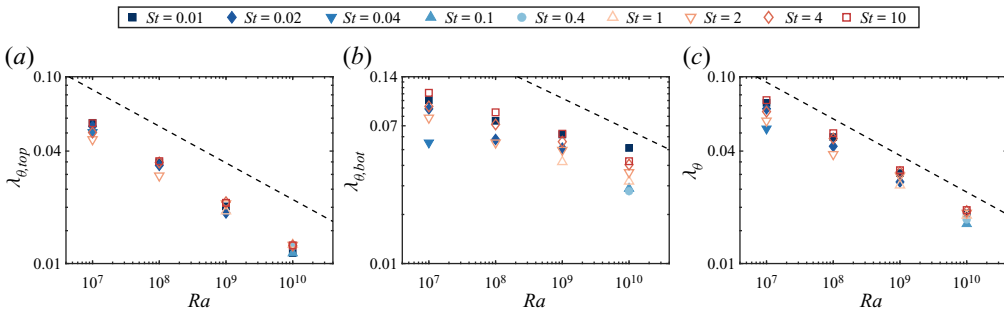


Figure 4. The thickness of (a) top thermal BL, (b) bottom thermal BL and (c) single thermal BL versus Rayleigh number. The dashed lines in the three panels have the same slope of  $-0.196$ .

$\lambda_{u,top} \sim Ra^{-0.196}$ , which is shown in figure 3(a). The thickness of the bottom BL  $\lambda_{u,bot}$  does not follow a single power-law scaling but shows complex dependence on  $Ra$ . Note that  $\lambda_{u,bot}$  is much larger than  $\lambda_{u,top}$ , which is consistent with the fact that the flow motions are stronger in the upper part of domain. Nevertheless, at larger  $Ra$ ,  $\lambda_{u,bot}$  starts to follow the same scaling law as that for  $\lambda_{u,top}$ .

The variations of  $\lambda_{\theta,top}$ ,  $\lambda_{\theta,bot}$  and  $\lambda_{\theta}$  are plotted in figure 4. Numerical results reveal that the thickness of the top thermal BL follows the same scaling law as  $\lambda_{u,top}$ , namely  $\lambda_{\theta,top} \sim Ra^{-0.196}$ , while the thickness of bottom thermal BL does not. Again,  $\lambda_{\theta,bot}$  is considerably larger than  $\lambda_{\theta,top}$ . The combined thickness  $\lambda_{\theta}$  shares the same scaling behaviour as  $\lambda_{\theta,top}$ . This is expected since by its definition,  $\lambda_{\theta}$  is dominated by  $\lambda_{\theta,top}$  which has smaller values than  $\lambda_{\theta,bot}$ . The power-law scaling for  $\lambda_{u,top}$  and  $\lambda_{\theta,top}$  will be used to explain the particle accumulation towards the top boundary for intermediate Stokes numbers.

Figure 5 shows the dependences of the volume-averaged temperature  $\langle \theta \rangle_V$  and the volume-averaged convective flux  $\langle w\theta \rangle_V$  on  $St$  for different  $Ra$ . Again, the two quantities are assumed to follow a certain power-law scaling about  $Ra$  and the exponents are determined by the same fitting method as for the BL thickness. The exponent is approximately 0.137 for  $\langle \theta \rangle_V$  and 0.084 for  $\langle w\theta \rangle_V$ , respectively. In figure 5(c,d) the  $Ra$ -compensated values are plotted versus  $St$ . Both  $\langle \theta \rangle_V$  and  $\langle w\theta \rangle_V$  first decrease and then increase as  $St$  increases from 0.01 to 10. The minima are expected to be reached approximately at  $0.1 \leq St \leq 0.4$ .

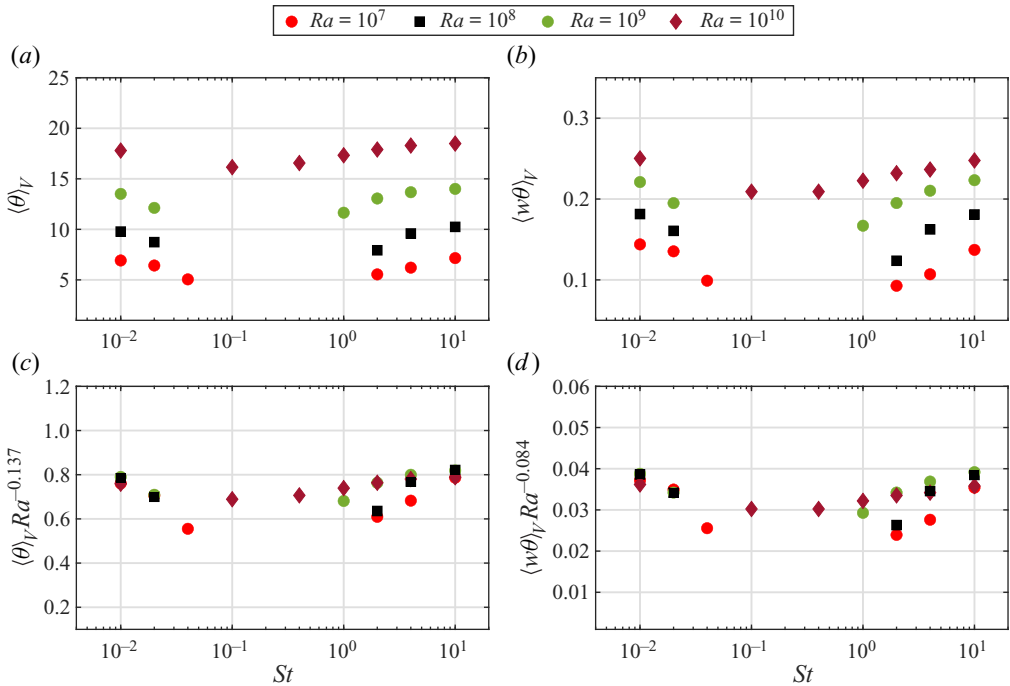


Figure 5. The dependences of (a) volume-averaged temperature  $\langle \theta \rangle_V$  and (b) volume-averaged convective flux  $\langle w\theta \rangle_V$  on the Stokes number  $St$  and Rayleigh number  $Ra$ . (c,d) The  $Ra$ -compensated plots of the same dataset.

### 3.3. Transport properties

For the current flows, the heat is extracted from the two cold walls from the top and bottom. For the pure conductive state with uniformly distributed particles, the heat flux should be the same at two boundaries. When flow motions exist, the heat flux is not even at the two plates. The asymmetry of heat flux between the two plates is measured by the fraction coefficient  $F_B$  defined in (2.11). Note that two mechanisms can contribute to  $F_B$ . The first one is of course the vertical flow motion, which is similar to the internally heated RB flow. The other one is the distribution of particles which affects the distribution of heating source.

To separate the two mechanisms, we make use of the temperature equation (2.14c) of the fluid phase. By taking the temporal and horizontal average for the statistically steady state, one has

$$\frac{d\langle w\theta \rangle_h}{dz} = Ra^{-1/3} Pr^{-1/3} \frac{d^2\langle \theta \rangle_h}{dz^2} + \langle q \rangle_h. \quad (3.4)$$

The above equation can be integrated twice, starting from the bottom plate, and gives

$$\langle w\theta \rangle_V = -Ra^{-1/3} Pr^{-1/3} \left. \frac{d\langle \theta \rangle_h}{dz} \right|_{bot} + \int_0^1 \int_0^z \langle q \rangle_h ds dz. \quad (3.5)$$

Then with the help of (3.2) and (3.3), one obtains

$$F_B = F_B^{turb} + F_B^{part}, \quad (3.6)$$

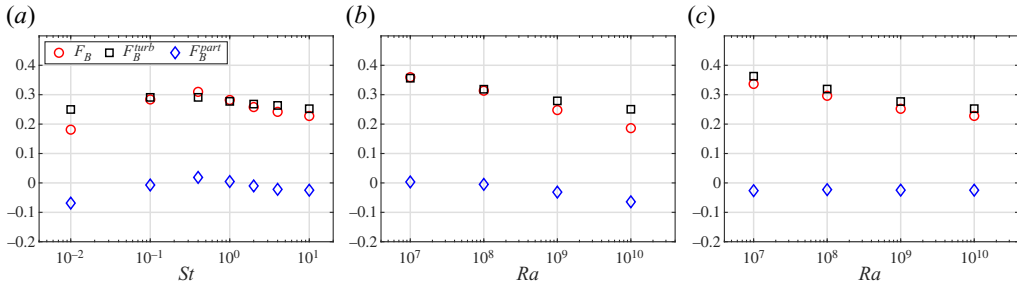


Figure 6. The variations of the fraction coefficient  $F_B$  and its two components versus the control parameters: (a) increasing  $St$  for fixed  $Ra = 10^{10}$ ; (b,c) increasing  $Ra$  for fixed  $St = 0.01$  and  $St = 10$ , respectively.

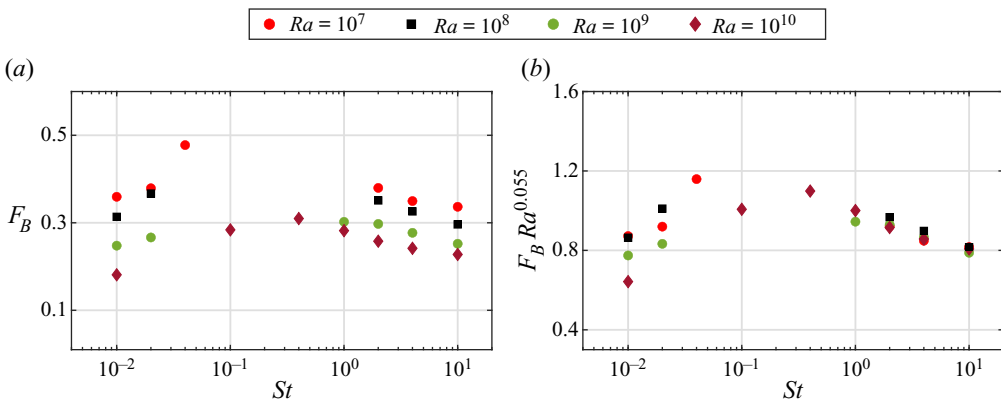


Figure 7. (a) The dependence of fraction coefficient  $F_B$  on the Stokes number  $St$  and Rayleigh number  $Ra$ . (b) The  $Ra$ -compensated plot of the same dataset.

with

$$F_B^{turb} = \frac{1}{2} - \langle w\theta \rangle_V, \quad F_B^{part} = \int_0^1 \int_0^z (\langle q \rangle_h - \langle q \rangle_V) ds dz. \quad (3.7a,b)$$

Note that  $F_B^{turb}$  is the same as in the internally heated RB (Goluskin & van der Poel 2016; Wang *et al.* 2020), while  $F_B^{part}$  is unique to the current system. In figure 6 we plot the variations of  $F_B$  and its two components for three groups of cases. Clearly,  $F_B$  is dominated by  $F_B^{turb}$ . For most cases the contribution  $F_B^{part}$  from particles is small and close to zero. For fixed  $Ra = 10^{10}$ ,  $F_B$  and the two components first increase and then decrease as  $St$  increases from 0.01 to 10. They reach the maximal values at  $St = 0.4$ . For the two fixed  $St$ ,  $F_B$  decreases as  $Ra$  increases, which is very similar to the three-dimensional (3-D) simulations of internally heated RBC of Goluskin & van der Poel (2016). Actually, Goluskin & van der Poel (2016) found out that  $F_B \sim Ra^{-0.055}$ . In figure 7 we plot the dependence of  $F_B$  on  $St$  for all simulated cases, and the compensated value  $F_B Ra^{0.055}$  versus  $St$ . The exponent is directly adopted from Goluskin & van der Poel (2016). The rescaling of  $F_B$  indeed collapses the data with different  $Ra$ , especially at the large  $St$  range.

We then turn to the scalings of Reynolds number and the volume-averaged temperature. Similar to Shraiman & Siggia (1990), we start from the exact balance between the viscous

dissipation rate and the convective flux, which can be readily obtained as

$$\epsilon_u = \nu \langle (\partial_i^* u_j^*)^2 \rangle_V = \frac{\nu^3}{H^4} RaPr^{-2} \langle w\theta \rangle_V. \quad (3.8)$$

Following the argument of the GL theory in RB flows (Grossmann & Lohse 2000, 2001, 2002, 2004), the total dissipation rate can be divided into the contributions from the BLs and the bulk, namely,

$$\epsilon_u = \epsilon_u^{BL,top} + \epsilon_u^{BL,bot} + \epsilon_u^{bulk}. \quad (3.9)$$

Here the top and bottom BLs are separated from each other, since as suggested by figure 3, the two BLs have different scaling behaviours. The scaling relations between the viscous dissipation rate and the Reynolds number are different for BL and bulk. In the framework of GL theory and assuming laminar BLs, the two scalings are

$$\epsilon_u^{BL} \sim \frac{\nu^3}{H^4} Re^{5/2}, \quad \epsilon_u^{bulk} \sim \frac{\nu^3}{H^4} Re^3. \quad (3.10a,b)$$

Moreover, for the convection flow with not very strong thermal driving, it is usually believed that the dissipation is dominated by the contribution from BL regions. For instance, Wang *et al.* (2020) reported that the BL contribution  $\epsilon_u^{BL}$  is dominant for  $Rr \leq 10^{11}$  in the two-dimensional (2-D) simulations of the internally heated convection. Here,  $Rr = (g\alpha\Omega H^5)/(\nu\kappa^2)$  is the Rayleigh–Robert number with  $\Omega$  being the strength of the uniform heat source.

However, the current system exhibits different behaviours. Figure 8 shows the mean profiles of  $\epsilon_u$  for increasing  $St$  and fixed  $Ra = 10^{10}$ . The dissipation rate is larger in the upper bulk due to the stronger fluid motions there. Meanwhile,  $\epsilon_u$  at bulk is consistently smaller for the intermediate Stokes numbers than that for small or large Stokes numbers, which is probably a consequence of the stronger preferential concentration at the intermediate Stokes numbers. In figure 9 we plot the dependences of dissipation rates on the Reynolds number for three regions. Clearly, the dissipation rate in the bulk region is much higher than those in the two BL regions. The exact physical reasons for the difference between the current flow and the internally heated convection with uniform source are not clear at this stage, but we do observe that the bulk has different morphology in the two systems. Goluskin & van der Poel (2016) has shown that there is no large-scale circulation in 3-D simulations of the uniformly heating RB. However, for the current system large-scale circulation is observed and shown in figure 10. In the figure the streamlines of the temporally averaged velocity field on the vertical midplane are displayed for three cases with  $Ra = 10^{10}$  and different  $St$ , and a pair of large-scale convection rolls are presented. Since heat-releasing particles are advected by convection motions, the spatial structures of the internal heat source can be very different from a uniform one, which is very likely to induce a different flow state. Interestingly, a very recent study (Kazemi, Ostilla-Mónico & Goluskin 2022) reveals that large-scale convection rolls can develop in the non-uniformly heating RB where the internal heating source has an exponential distribution. All these different studies imply that the flow morphology in the bulk strongly depends on the spatial distribution of heating source in the internally heating RB flows.

Nevertheless, by using the fact that the dissipation rate is dominated by the bulk contribution, and employing the power-law scaling in figure 9(c), one obtains the following

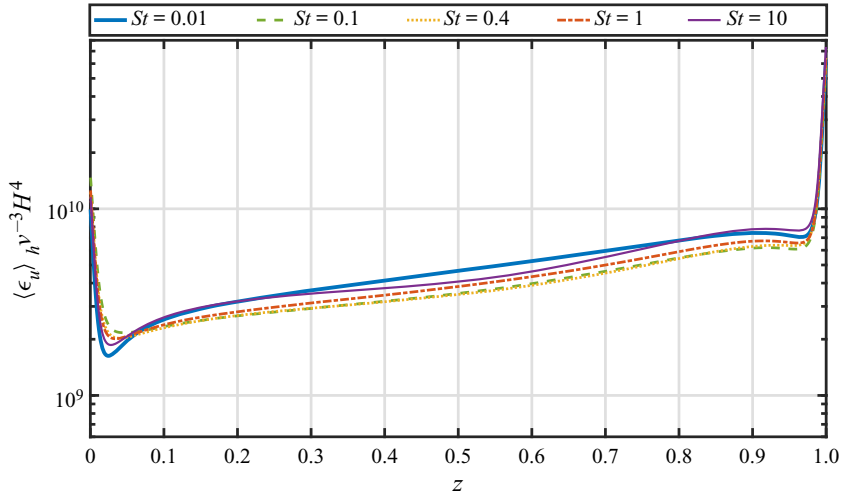


Figure 8. The mean profiles of the viscous dissipation rate  $\langle \epsilon_u \rangle_h$  versus the height  $z$  for different  $St$  and fixed  $Ra = 10^{10}$ .

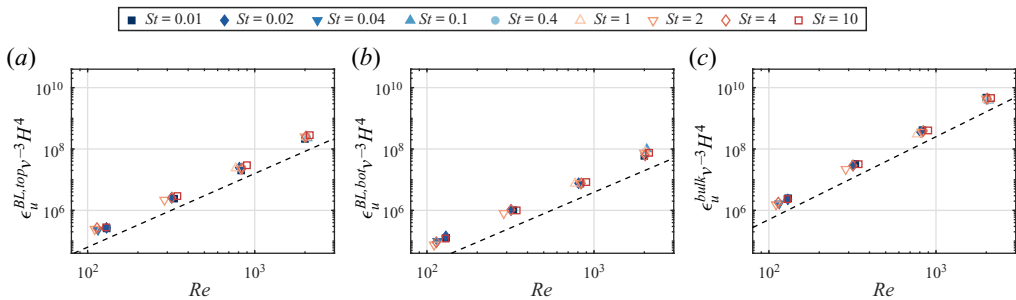


Figure 9. The total dissipation rate in (a) the top BL region, (b) the bottom BL region and (c) the bulk versus the Reynolds number, respectively. In panels (a–c) the slope of the dashed line is 2.4, 2.33 and 2.7, respectively.

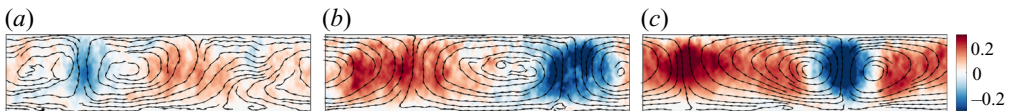


Figure 10. The temporally averaged flow field on a vertical midplane. Contours show the vertical velocity, and the streamlines are integrated with the in-plane velocity vector. Here (a)  $St = 0.01$ , (b)  $St = 0.4$ , and (c)  $St = 10$ , respectively, and the Rayleigh number is  $Ra = 10^{10}$ .

scaling relation:

$$Re^{2.7} \sim \epsilon_u^{bulk} \frac{H^4}{\nu^3} \approx Ra Pr^{-2} \langle w\theta \rangle_V. \quad (3.11)$$

We have also shown that  $\langle w\theta \rangle_V \sim Ra^{0.084}$ , which implies that

$$Re \sim Ra^{0.40} Pr^{-3/2}. \quad (3.12)$$

In figure 11 the above scaling is compared with the numerical results and the agreement is very good. Moreover, for laminar BL one has  $\lambda_u \sim Re^{-1/2} \sim Ra^{-0.2}$ , which is also

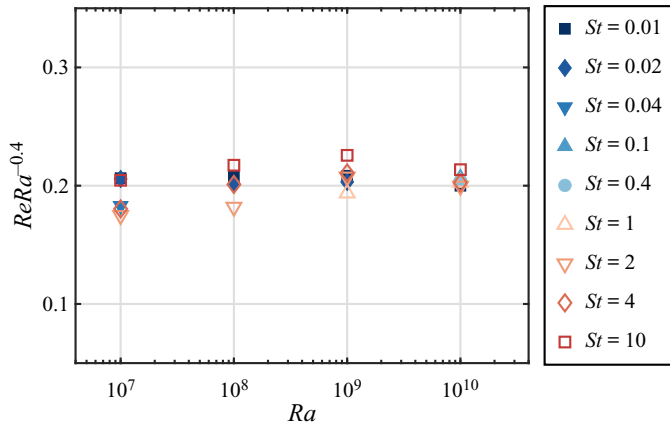


Figure 11. The compensated plot of Reynolds number  $Re$  versus  $Ra$ .

very close to the scaling of the top BL thickness in figure 3(a). For the volume-averaged temperature  $\langle \theta \rangle_V$ , we note that the total heat flux from two boundaries can be approximated as  $\langle \theta \rangle_V / \lambda_\theta$ . For laminar BLs  $\lambda_\theta \sim \lambda_u Pr^{-1/3} \sim Re^{-1/2} Pr^{-1/3}$ . Then by using (3.3), one has

$$\langle \theta \rangle_V \sim Ra^{1/3} Pr^{1/3} \lambda_\theta \sim Ra^{0.133} Pr^{2/5}. \quad (3.13)$$

The exponent 0.133 is also close to that given by the linear fitting, see figure 5(c).

#### 4. Particle distributions and different flow regimes

With the help of the flow characteristics and transport properties discussed in the previous section, the spatial distribution of particles will be investigated in this section. We first identify the boundaries of the flow regime where the consistency between simulation results and physical models holds, and then discuss the preferential concentration of particles for those cases with a statistically steady state.

##### 4.1. Particle accumulation and different flow regimes

For some cases at  $Ra \leq 10^9$  and certain range of  $St$ , as mentioned before and indicated by the black diamonds in figure 1, most particles will eventually accumulate into a thin layer adjacent to the top plate, where the local heating intensity is very strong. If the time step is reduced, the simulation can continue for longer time period. But eventually the time step becomes extremely small and the simulation is unfeasible. Outside this regime the flow can reach a statistically steady state in several hundreds of non-dimensional time units. The heat released from particles drives the convection flow which transport particles over the whole domain. The local particle number density remains small at all heights and the physical models we employed are still valid.

To illustrate these different states, we uniformly divide the flow domain into 40 slabs along the vertical direction. The mean number density  $c_s$  is then calculated for each slab and normalized by the initial mean number density of the entire domain. Therefore, if all particles stay in a single slab, this slab will have  $c_s = 40$ . In figure 12 we plot the time history of the profile  $c_s$  for two cases with  $Ra = 10^9$  from different regimes. For the case with  $St = 0.1$ , at approximately 100 time units  $c_s$  is very close to 40 for the slab adjacent to the top plate, indicating that almost all particles stay within this thin layer at the top. The



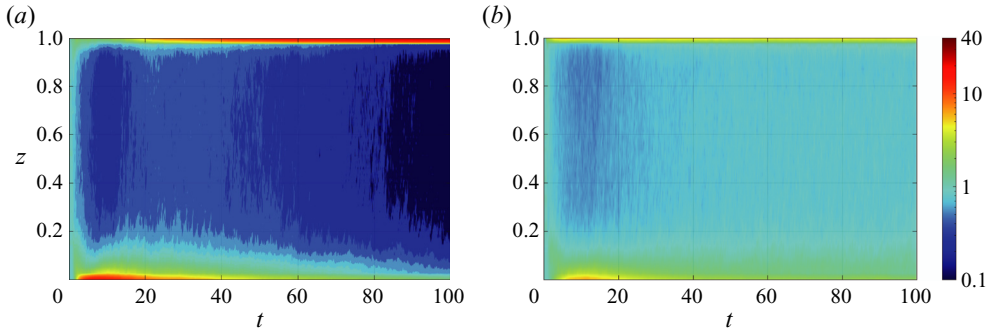


Figure 12. The time evolution of the profile of mean number density of particles for two cases with (a)  $St = 0.1$  and (b)  $St = 0.02$ , respectively. The Rayleigh number  $Ra = 10^9$  is same for the two cases.

simulation has to stop at approximately  $t = 120$  due to the extreme large heating source close to the top boundary. Meanwhile, for the case with  $St = 0.02$ ,  $c_s$  is still higher at the slabs close to the top and bottom plates, but in the bulk  $c_s$  does not approach zero. Particles can still travel inside the bulk region for this case, and finally a statistically steady state is established.

For some cases close to the regime where the particle accumulation happens, flow can still reach a statistically steady state and the simulation can continue. However, the normalized number density is elevated over 10 within the upper viscous BL adjacent to the top boundary. These cases are marked by the yellow squares in figure 1. Therefore, the transitions between these two regimes on the  $St-Ra$  phase plane are not sharp ones, and can be roughly understood as follows. Two processes are responsible for the left-hand and right-hand transition boundaries in the phase space. For the first process, one can start from the large Stokes number where a statistically steady state exists. With large enough  $St$ , particles which enter the top boundary layer cannot decelerate and stop moving in the vertical direction within the top BL. As  $St$  decreases, particles become more responsive to the change of fluid momentum. If the vertical velocity of particles can decrease to zero before particles penetrate the top BL, they will be trapped inside the BL region. For the second process, one starts from the small Stokes number where again a statistically steady state exists. Now because particles can perfectly follow the flow motions, they are carried out of the top BL by the descending plumes. However, as  $St$  increases, particles become less responsive and they may not gain enough downward velocity to escape the top BL during the time period as they travel over the height of the top BL. In the following we establish the scaling laws for the transition boundaries based on the two processes.

For the first process, we notice that inside the viscous BL next to the top plate, the vertical velocity component  $w_f$  is small compared with the horizontal velocity component. As an approximation we take  $w_f \approx 0$ . When a particle enters the BL with a certain vertical velocity  $w_p^0$ , the vertical velocity of the particle will decrease due to the vertical component of the Stokes drag. From (2.14e) one obtains a formal solution as

$$w_p(t) = w_p^0 \exp(-t/St). \tag{4.1}$$

Then the total height which the particle travels until  $w_p$  reaches zero is given by

$$\delta z_p = \int_0^\infty w_p(t) dt = \int_0^\infty w_p^0 \exp(-t/St) dt = w_p^0 St. \tag{4.2}$$

If  $w_p$  decreases to zero before the particle moves through the height of BL, i.e.  $\delta z_p \leq \lambda_{u,top}$ , then the particle will stay within the BL. This gives a scaling relation of the minimum particle entry velocity  $w_{p,min}^0$  for a particle to travel into and through the BL:

$$w_{p,min}^0 St \sim \lambda_{u,top}. \tag{4.3}$$

In the previous section we have shown that  $\lambda_{u,top} \sim Re^{-1/2}$  and  $Re \sim Ra^{2/5}$ .

Meanwhile, the entry velocity  $w_p^0$  should have the same order as the velocity scale in the bulk, namely  $w_p^0 \sim U_{rms} \sim Re$ . When the particles are trapped in the BL by a drag force, the entry velocity  $w_p^0$  should be smaller than  $w_{p,min}^0$ . The critical Stokes number  $St_{cr}^u$  can be obtained when  $w_p^0 \sim w_{p,min}^0$ . Thus, one has

$$St_{cr}^u \sim \lambda_u/w_p^0 \sim Re^{-3/2} \sim Ra^{-3/5}. \tag{4.4}$$

Since for fixed  $Ra$  and therefore fixed  $\lambda_u$ ,  $\delta z_p$  increases as  $St$  becomes larger. The first process is effective when  $St < St_{cr}^u$ , and particles with smaller  $St$  will stay inside the BL while those with larger  $St$  will not. This suggests that  $St_{cr}^u$  corresponds to the upper transition boundary between two regimes.

For the second process, as the particles already inside the BL cannot escape, we point out that particles escaping the top BL are mainly carried downwards by the cold plumes ejected from the top BL. The time scale for a fluid element to move through the BL can be estimated as  $\tau_f^{bl} \sim \tau_f \lambda_{u,top}/H$ , in which we assume that the fluid element moves through the entire domain height  $H$  with the time scale  $\tau_f$ . When  $\tau_p < \tau_f^{bl}$ , particles will gain a vertical downward velocity close enough to fluid velocity and are likely to be transported away from the BL. Then a scaling relation for this transition is  $\tau_p/\tau_f^{bl} \sim 1$ . Recalling that  $\lambda_{u,top} \sim Ra^{-1/5}$ , one obtains

$$St_{cr}^l \sim Ra^{-1/5}. \tag{4.5}$$

For the second process to be effective, the Stokes number should be larger than  $St_{cr}^l$ , and the above scaling corresponds to the lower transition boundary between the two regimes.

The two scaling relations (4.4) and (4.5) for the transition boundaries between different regimes are plotted in figure 1 with properly chosen prefactors. The above two mechanisms are both necessary for particles to accumulate in the BL, which means the Stokes number should satisfy  $St_{cr}^l \leq St \leq St_{cr}^u$ . As can be seen from figure 1, the predictions given by the above scaling analyses capture the transition boundaries every well.

#### 4.2. Preferential concentration of particles and mean statistics

When the flow reaches the final statistically steady state, particles still exhibit preferential concentration. We first look at the vertical distribution of particles. In figure 13 we show the instantaneous flow fields and particle distributions on a vertical plane for three cases with the same  $Ra = 10^{10}$  and increasing  $St = 0.01, 0.4$  and  $10$ , respectively. For the two cases with small or large  $St$ , particles are fairly uniform in the bulk. Due to the nearly uniform distribution in the bulk, the fluid temperature is also relatively high as particles are heating the fluid. However, for the case with intermediate  $St$ , particles show

Wall-bounded turbulent driven by heat-releasing particle

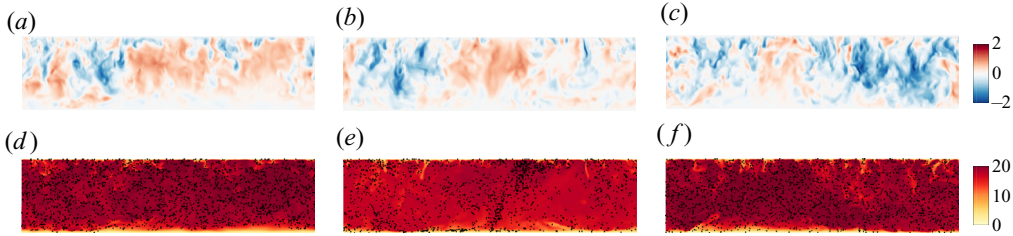


Figure 13. (a–c) The contours of vertical velocity on a middle vertical plane, and (d–f) the contours of temperature field along with the instantaneous particle distribution on the same vertical plane, respectively. Here (a,d), (b,e) and (c,f) are  $St = 0.01, 0.4$  and  $10$ , respectively. The Rayleigh number is  $Ra = 10^{10}$ .

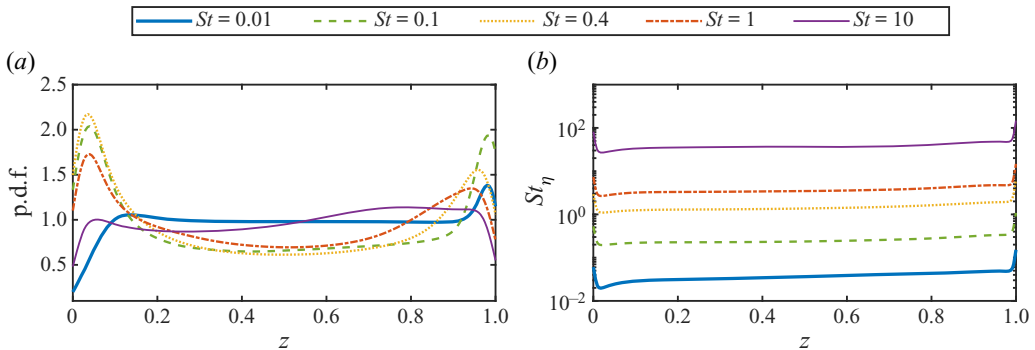


Figure 14. (a) The probability density function of the vertical positions of particles. (b) The Stokes number  $St_\eta$  defined by the local Kolmogorov time scale versus the height. For all the shown cases  $Ra = 10^{10}$ .

clear non-uniform distribution. The number density is higher near the top and bottom boundaries, and inside the rising flow in the bulk, as can be seen by comparing figure 13(b) and figure 13(e).

To quantitatively measure the possible non-uniform distribution along the vertical direction, figure 14(a) plots the probability density function (p.d.f.) of the vertical location  $z$  of particles for the five cases with fixed  $Ra = 10^{10}$  and different  $St$ . For the largest  $St = 10$  and the smallest  $St = 0.01$ , the p.d.f. is lower near the bottom boundary, and higher near the top boundary. The difference is that for  $St = 0.01$ , the p.d.f. has a single peak close to the top boundary. While for  $St = 10$ , the high p.d.f. happens in a wider region without an apparent peak near the top. For the three intermediate Stokes numbers, their p.d.f.s all have two peaks located close to the top and bottom plates, and are relatively low in the bulk, indicating stronger non-uniformity along the vertical direction. The fact that p.d.f. is the lowest in the bulk for  $St = 0.1$  and  $0.4$  is consistent with the behaviours shown in figure 5. Since particles release heat to the surrounding fluid, lower number density in the bulk corresponds to weaker heating source and volume-averaged temperature is also smaller.

The different shapes of p.d.f.s for different  $St$  can be understood as follows. In figure 14(b) we plot the vertical profiles of  $St_\eta = \tau_p/\tau_\eta$  with  $\tau_\eta = \eta_u^2/\nu$  being the local Kolmogorov time scale. Here  $\eta_u$  is the Kolmogorov length scale calculated at each height. Here  $St_\eta$  is slightly larger than  $St$  in all cases. Still, for  $St = 0.01$  and  $10$ ,  $St_\eta$  is far away from unit and the momentum coupling between flow and particles is weak. When

$St = 0.01$  the particles follow the fluid almost perfectly. Since particles release heat into the surrounding fluid, particles are more likely to rise towards the top plate, and stay at the top until being carried away by the downward plumes. For  $St = 10$ , the particle inertia is very large and their movement is hardly affected by the flow. They prefer to move upward due to the heat-releasing effect. But when they move towards the top plate, they can easily penetrate the BL, rebound at the top boundary, and then leave the top BL due to the large inertia. Therefore, p.d.f. does not have a peak near the top plate as in the case with  $St = 0.01$ . For the other three cases,  $St_\eta$  is close to unity and the momentum coupling is strong between the fluid flow and the particles. It is well known that the preferential concentration is most distinct for  $St_\eta \approx 1$  in turbulent channel flows (Sardina *et al.* 2012). Also as discussed in the previous section, for the cases with intermediate  $St$ , particles are more likely to be trapped within the BL regions where the vertical velocity is small.

The preferential concentration in the horizontal directions is examined by the Voronoï diagrams (Ferenc & Néda 2007; Monchaux, Bourgoin & Cartellier 2010; Yang *et al.* 2021). That is, the horizontal plane is divided into Voronoï cells based on particle locations. The area  $A$  of the Voronoï cell associated with each particle is inversely correlated to the local concentration of particles. We choose three horizontal planes at the edges of two viscous BLs and  $z/H = 0.5$ . Typical Voronoï diagrams on these planes are shown in figure 15 for three cases with fixed  $Ra = 10^{10}$  and  $St = 0.01, 0.4$  and  $10$ , respectively. For  $St = 0.4$ , the preferential concentration is strongly presented in all three heights. Small clusters form large clusters which non-uniformly distribute over the horizontal planes. For  $St = 10$ , small clusters can be observed but they do not form large clusters, but randomly distribute over the plane. For  $St = 0.01$ , the behaviours are similar to those with  $St = 10$  at the mid plane and the edge of top viscous BL. However, large voids with nearly no particles form at the edge of bottom viscous BL. This is because particles with  $St = 0.01$  are more likely to be carried away from the bottom viscous BL by fluid motions.

The p.d.f.s of the area of Voronoï cells are sampled at three different heights and plotted in figure 16 for different Stokes numbers and fixed  $Ra = 10^{10}$ . The p.d.f. for a random Poisson process (RPP), which corresponds to the uniformly random distribution of particles, is shown for comparison. For all three heights, the right-hand tails of the p.d.f.s approach the RPP distribution as  $St$  becomes larger, while a flat tail always exists on the left-hand side. Moreover, the left-hand tails exhibit different behaviours at different heights as  $St$  increases. For both the midheight and the edge of the top BL, p.d.f. at small  $A/\langle A \rangle_p$  is highest at the intermediate Stokes numbers, indicating the strongest preferential concentration due to the momentum interaction between fluid and particles. At the edge of the bottom BL, the p.d.f. of the smallest  $St = 0.01$  has the highest left-hand tail, consistent with the distribution shown in figure 15(a–c).

Figure 17 displays the p.d.f.s of the area of Voronoï cells for two fixed  $St$  and increasing  $Ra$  at three heights. For  $St = 0.01$ , the clustering at the edge of the bottom BL becomes stronger as  $Ra$  increases, as indicated by the elevation of the left-hand tails in figure 17(a). Meanwhile, the right-hand tails deviate from the RPP distribution. At the midheight and the edge of top BL, the influence of increasing  $Ra$  is much smaller. For  $St = 10$ , the p.d.f. does not change much with  $Ra$  at all three heights. The right-hand tails are very close to the RPP distribution, and the flat left-hand tails are produced by the small clusters shown in figure 15.

To quantitatively investigate the multiscale nature of particle clusters on horizontal planes, we employ the radial distribution functions (RDF) (e.g. Ireland, Bragg & Collins

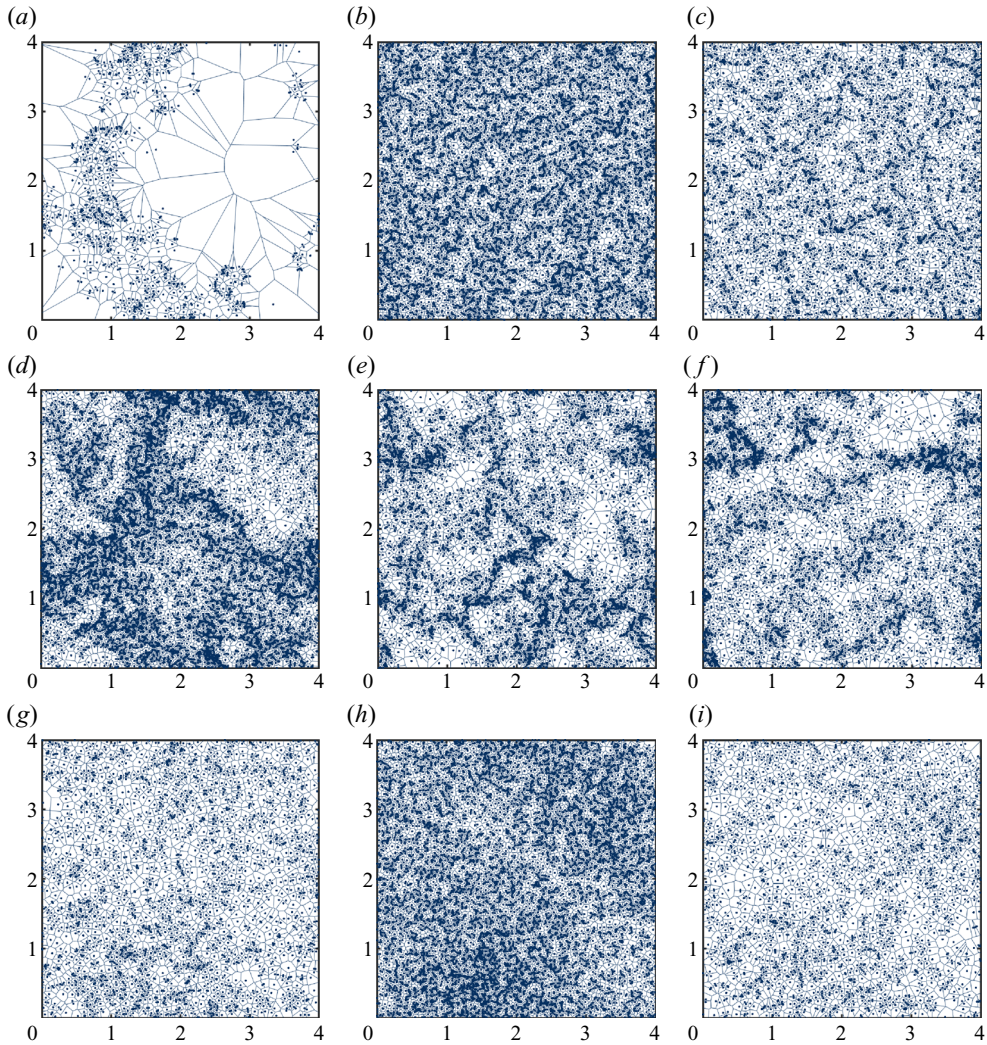


Figure 15. Typical snapshots of the horizontal distribution of particles and their Voronoï diagram for  $Ra = 10^{10}$  and different  $St$ : (a–c)  $St = 0.01$ ; (d–f)  $St = 0.4$ ; (g–h)  $St = 10$ . Here (a,d,g), (b,e,h) and (c,f,i) are  $z = \lambda_{u,bot}, 0.5H, H - \lambda_{u,top}$ , respectively.

2016). The RDF  $g(r)$  is calculated by

$$g(r) = \frac{N_r/V_r}{N/V}. \quad (4.6)$$

Here,  $N_i$  is the number of particle pairs whose separation distances fall inside the shell with a radius range  $(r - \Delta r/2, r + \Delta r/2)$ . Here  $V_r$  is the volume of the corresponding shell in the distance space,  $N$  is the total number of particle pairs and  $V$  is the total volume. When  $g(r)$  is equal to 1, the particle field is uniformly distributed. Here  $g(r)$  greater than unity indicates a clustered particle field at scale  $r$ .

The 2-D RDFs are computed over the horizontal slices at  $z = \lambda_{u,bot}$ ,  $z = 0.5H$  and  $z = H - \lambda_{u,top}$  for fixed  $Ra = 10^{10}$  and different  $St$ , which are shown in figure 18. At the lower slice shown,  $g(r)$  is considerably larger than 1 for almost all the computed

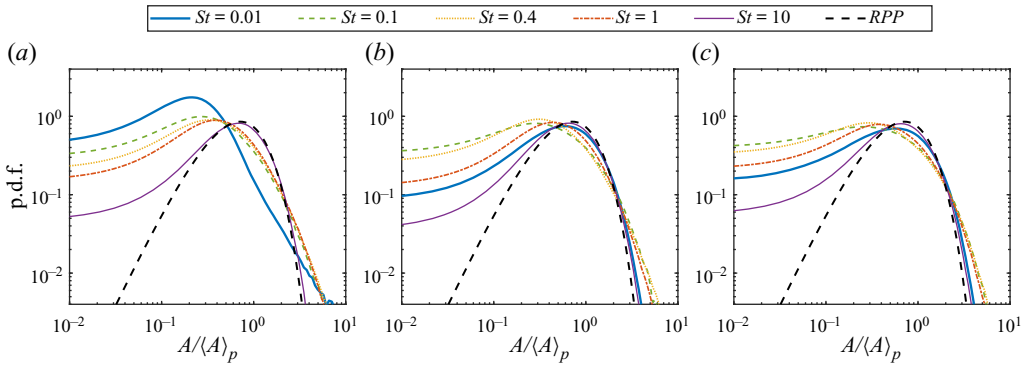


Figure 16. The p.d.f.s of normalized Voronoi area  $A/\langle A \rangle_p$  in the horizontal planes for different  $St$  and  $Ra = 10^{10}$ : (a)  $z = \lambda_{u,bot}$ ; (b)  $z = 0.5H$ ; (c)  $z = H - \lambda_{u,top}$ .

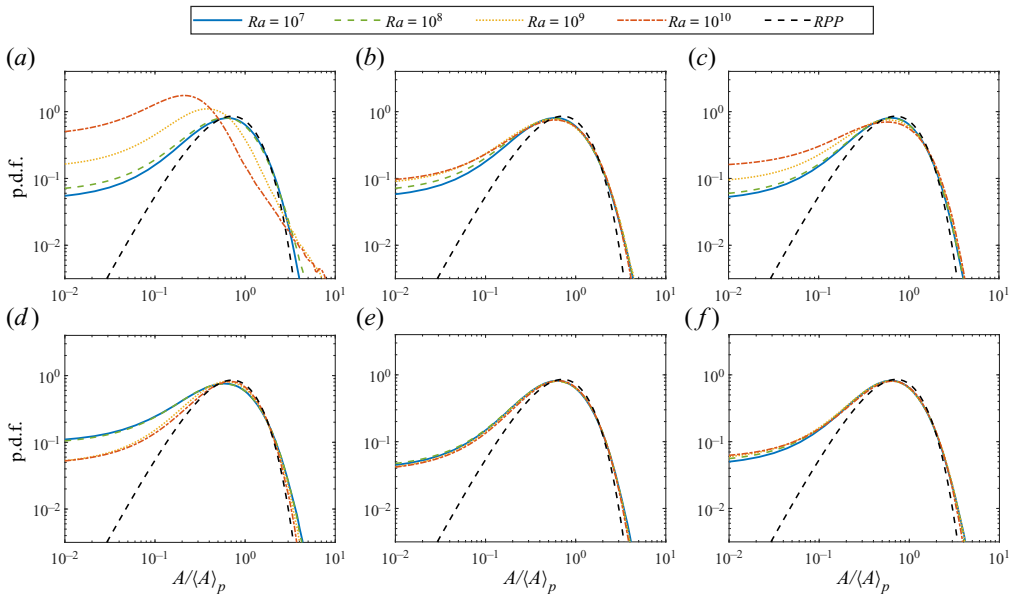


Figure 17. The p.d.f.s of normalized Voronoi area  $A/\langle A \rangle_p$  in the horizontal planes for different  $St$  and  $Ra$ : (a,d)  $z = \lambda_{u,bot}$ ; (b,e)  $z = 0.5H$ ; (c,f)  $z = H - \lambda_{u,top}$ . Here panels (a–c) are for  $St = 0.01$ , and (d–f) for  $St = 10$ , respectively.

distance  $r$  at  $St = 0.01$ , corresponding to the large voids shown in figure 15(a). As  $St$  increases,  $g(r)$  gradually decreases at nearly all  $r$ . This is consistent with figure 15(a,d,g), where large voids at  $St = 0.01$  transit into large clusters at  $St = 0.4$  and then nearly uniformly distributed small clusters at  $St = 10$ . At the two higher slices with  $z = 0.5H$  and  $H - \lambda_{u,top}$ ,  $g(r)$  experiences non-monotonic variations as  $St$  becomes larger. Now  $g(r)$  exceeds unity over wider range of  $r$  for intermediate  $St$ , indicating again the preferential distribution with large clusters formed by small clusters.

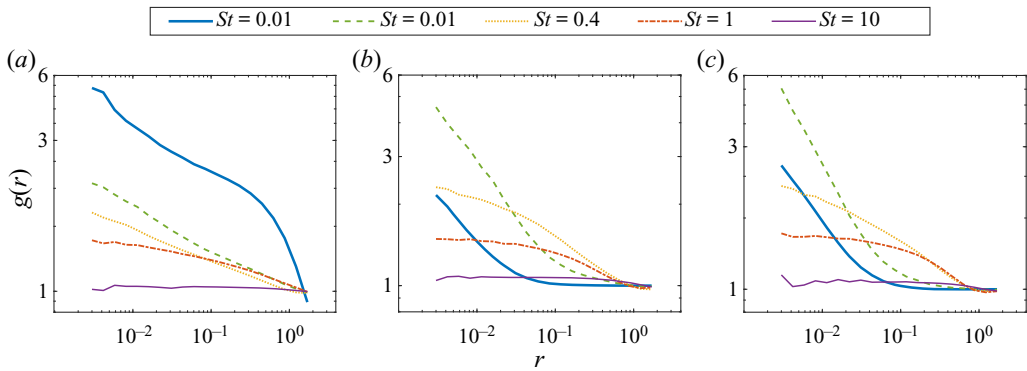


Figure 18. The RDFs in the horizontal planes for different  $St$  and fixed  $Ra = 10^{10}$ : (a)  $z = \lambda_{u,bot}$ ; (b)  $z = 0.5H$ ; (c)  $z = H - \lambda_{u,top}$ .

## 5. Conclusions

In this work we conducted a systematic study of the convection flow driven by heat-releasing point particles which absorb energy from an external source. The energy absorbed by particles is then released to heat the surrounding fluid, which drives the buoyancy flow motions in the domain. The heat is then transferred out from the domain through the top and bottom plates. We confine ourselves within the parameter space where the global volume fraction of particles is small and the Froude number is large, so that one-way coupling is used for momentum interaction and two-way coupling for thermal interaction, respectively. Meanwhile, the gravitational settling of particles is neglected. The current study then focuses on the influences of the Rayleigh number  $Ra$  within the range  $(10^7, 10^{10})$  and the Stokes number  $St$  within the range  $(0.01, 10)$ , while the other non-dimensional numbers are fixed.

Within the parameter range simulated here, we reveal a regime in which nearly all the particles will eventually accumulate towards the top plate. We identify the physical mechanism of this accumulation as the interaction between the inertial particles and the top BL. Specifically, for intermediate Stokes numbers at certain Rayleigh number, the particles do not respond to the fluid motion quickly enough and cannot be carried away from the BL. Meanwhile, their inertia is not too strong to fully decouple with the flow within the BL. By scaling analyses we propose the upper and lower boundaries in the  $Ra - St$  phase plane, which can describe the numerical results perfectly. Outside this regime, the flow can reach a statistically steady state with particles constantly advected over the entire domain.

For the flow at a statistically steady state, the flow and mean statistics are asymmetric between the upper and lower parts of the domain. The flow motions are stronger in the upper part of bulk region, and the top BL is thinner than the bottom one for both momentum and temperature fields. Both the volume-averaged temperature and convective heat flux exhibit non-monotonic dependences on  $St$  and their minima are expected to locate at  $0.1 \leq St \leq 0.4$ . The fraction coefficient  $F_B$ , which measures the asymmetry between the heat fluxes through the top and bottom plates, is dominated by the convective flux. Our numerical results indicate that the dependences of both the convective flux and  $F_B$  on  $Ra$  are similar to those reported for internally heated RB with a uniform source.

However, our investigations also reveal several behaviours which are different from the internally heated RB with a uniform source. The viscous dissipation rate is dominated by the contribution from the bulk, while for uniformly heated RB with similar driving strength, the dominant contribution comes from the BLs. Also, in the current flow large-scale convection rolls develop in the bulk which were not found in the 3-D simulations of uniformly heated RB (Goluskin & van der Poel 2016). Nevertheless, by using the global balance between the dissipation rate and the convective flux and by adopting the relation extracted from the numerical data, the scaling behaviours of the Reynolds number, the volume-averaged temperature and the thicknesses of BLs can be explained.

Preferential concentration is also observed in the present flow. For intermediate Stokes numbers, particles have higher number density in both the top and bottom viscous BLs. In the horizontal directions the clustering of particles has a multiscale nature: the horizontal RDFs exceed unity over a wide range of particle separation distance at planes with different height. For small and large Stokes numbers, the multiscale clustering in the horizontal directions is much weaker. It should be pointed out, though, for the smallest Stokes number large voids with very low particle number density were observed over the horizontal plane near the bottom plate. Since the local strength of heating source strongly depends on the local particle concentration, the preferential concentration should have profound influences on the convection motions. This may explain the differences between the present flow and the uniformly heated RB.

The current work opens up several interesting directions for future study. For instance, two-way coupling in the momentum interaction can be included and the gravitational settling of particles may be considered. Note that gravitational settling and the heat-releasing to the surrounding fluid have competing effects on the vertical translation of particles, and non-trivial behaviours can be expected when the gravitational settling process is introduced in the system. These are the subjects of our ongoing research.

**Fundings.** This work is financially supported by the Marine S&T Fund of Shandong Province for Pilot National Laboratory for Marine Science and Technology (Qingdao) (no. 2022QNLM010201) and the Major Research Plan of National Natural Science Foundation of China for Turbulent Structures under the grants 91852107.

**Declaration of interests.** The authors report no conflict of interest.

**Author ORCIDs.**

 Yantao Yang <https://orcid.org/0000-0001-5065-2769>.

## Appendix A. Numerical details



$Ra$	$St$	$N_x$	$N_z$	$F_B$	$Re$	$\langle \theta \rangle_V$	$\lambda_u^{top}$	$\lambda_u^{bot}$	$\lambda_\theta$	$c_s^{top}$	$\langle \theta_p - \theta_f \rangle_p$	$Nu$
$10^7$	0.01	192	192	0.359	130.2	6.92	0.0290	0.0363	0.0725	1.33	0.999	0.995
$10^7$	0.02	192	192	0.379	129.8	6.42	0.0293	0.0381	0.0674	2.05	1.00	0.988
$10^7$	0.04	192	288	0.477	115.5	5.05	0.0298	0.0412	0.0526	4.61	1.00	0.997
$10^7$	0.08	192	288	—	—	—	—	—	—	18.8	0.999	0.978
$10^7$	0.1	192	192	—	—	—	—	—	—	—	—	—
$10^7$	0.4	192	192	—	—	—	—	—	—	—	—	—
$10^7$	1	192	192	—	—	—	—	—	—	—	—	—
$10^7$	2	192	288	0.379	110.3	5.54	0.0288	0.0387	0.0580	5.10	0.999	0.983
$10^7$	4	192	192	0.349	113.8	6.21	0.0303	0.0373	0.0650	3.81	1.00	0.976
$10^7$	10	192	192	0.336	129.1	7.15	0.0310	0.0378	0.0749	1.66	1.00	0.988
$10^8$	0.01	288	192	0.313	329.3	9.77	0.0185	0.0266	0.0475	1.71	1.00	0.992
$10^8$	0.02	288	192	0.367	318.7	8.73	0.0189	0.0287	0.0424	2.98	1.00	0.987
$10^8$	0.04	288	288	—	—	—	—	—	—	10.5	1.00	0.987
$10^8$	0.08	288	192	—	—	—	—	—	—	—	—	—
$10^8$	0.1	288	192	—	—	—	—	—	—	—	—	—
$10^8$	0.4	288	192	—	—	—	—	—	—	—	—	—
$10^8$	1	288	288	—	—	—	—	—	—	23.3	1.00	1.00
$10^8$	2	288	192	0.335	291.7	8.31	0.0200	0.0269	0.0412	7.52	1.00	0.985
$10^8$	4	288	192	0.326	318.7	9.59	0.0198	0.0252	0.0467	2.74	0.999	0.972
$10^8$	10	288	192	0.296	344.4	10.2	0.0207	0.0310	0.0498	1.47	1.00	0.988
$10^9$	0.01	432	192	0.247	829.5	13.5	0.0117	0.0225	0.0304	2.91	1.00	0.993
$10^9$	0.02	432	192	0.266	808.8	12.1	0.0122	0.0232	0.0273	8.11	1.00	0.995
$10^9$	0.04	432	192	—	—	—	—	—	—	—	—	—
$10^9$	0.1	432	192	—	—	—	—	—	—	—	—	—
$10^9$	0.4	432	288	—	—	—	—	—	—	21.4	0.999	1.02
$10^9$	1	432	192	0.322	791.2	11.7	0.0129	0.0226	0.0270	9.48	0.999	0.993
$10^9$	2	432	192	0.297	826	13.1	0.0128	0.0229	0.0295	3.11	1.00	0.980
$10^9$	4	432	192	0.277	839	13.7	0.0126	0.0228	0.0308	1.73	1.00	0.991
$10^9$	10	432	192	0.252	898.4	14.0	0.0132	0.0265	0.0315	1.16	1.00	0.993
$10^{10}$	0.01	648	288	0.181	2000	17.8	0.00739	0.0163	0.0186	4.94	1.00	1.00
$10^{10}$	0.02	648	288	—	—	—	—	—	—	10.2	1.00	1.00
$10^{10}$	0.04	648	288	—	—	—	—	—	—	14.9	1.00	1.00
$10^{10}$	0.1	648	288	0.283	2068	16.1	0.00818	0.0151	0.0163	9.39	1.00	1.03
$10^{10}$	0.4	648	288	0.309	2041	16.5	0.00835	0.0157	0.0172	3.06	1.00	1.00
$10^{10}$	1	648	288	0.282	2028	17.3	0.00804	0.0152	0.0181	1.67	0.999	1.00
$10^{10}$	2	648	288	0.258	1997	17.9	0.00799	0.0153	0.0186	1.29	1.00	0.999
$10^{10}$	4	648	288	0.242	2024	18.3	0.00792	0.0167	0.0191	1.20	1.00	1.00
$10^{10}$	10	648	288	0.227	2135	18.4	0.00814	0.0170	0.0193	0.980	1.00	1.00

Table 1. Summary of the numerical simulations. Columns from left to right are the Rayleigh number, the Stokes number, the resolutions in the horizontal and vertical directions, the fraction of internally heat across bottom boundaries, the Reynolds number based on the r.m.s. value of velocity, the mean system temperature, the thickness of top and bottom viscous BL, the thickness of temperature BL, the mean concentration  $c_s$  for the top BL, the mean temperature difference of two phases, the non-dimensional total heat flux across top and bottom plates  $Nu$ , respectively. The resolution in the  $y$  direction is the same as that in the  $x$  direction. For all cases the aspect ratio of the domain  $L = 4$ , the Prandtl number  $Pr = 0.7$ , the non-dimensional particle number density  $C = 1 \times 10^5$ , the heat-capacity ratio  $\Phi_\theta = 0.1$  and the heat-mixing parameter  $\sigma = 1$ .

REFERENCES

BALACHANDAR, S. & EATON, J.K. 2010 Turbulent dispersed multiphase flow. *Annu. Rev. Fluid Mech.* **42** (1), 111–133.  
 BANKO, A.J., VILLAFANE, L., KIM, J.H. & EATON, J.K. 2020 Temperature statistics in a radiatively heated particle-laden turbulent square duct flow. *Intl J. Heat Fluid Flow* **84**, 108618.

- BOUILLAUT, V., LEPOT, S., AUMAÎTRE, S. & GALLET, B. 2019 Transition to the ultimate regime in a radiatively driven convection experiment. *J. Fluid Mech.* **861**, R5.
- CREYSSELS, M. 2020 Model for classical and ultimate regimes of radiatively driven turbulent convection. *J. Fluid Mech.* **900**, A39.
- CROWE, C.T. 1982 Review – numerical models for dilute gas-particle flows. *J. Fluids Engng* **104** (3), 297–303.
- CUZZI, J.N., HOGAN, R.C., PAQUE, J.M. & DOBROVOLSKIS, A.R. 2001 Size-selective concentration of chondrules and other small particles in protoplanetary nebula turbulence. *Astrophys. J.* **546** (1), 496.
- DRITSELIS, C.D. & VLACHOS, N.S. 2011 Large eddy simulation of gas-particle turbulent channel flow with momentum exchange between the phases. *Intl J. Multiphase Flow* **37** (7), 706–721.
- DU, Y., ZHANG, M. & YANG, Y. 2021 Two-component convection flow driven by a heat-releasing concentration field. *J. Fluid Mech.* **929**, A35.
- DU, Y., ZHANG, M. & YANG, Y. 2022 Thermal convection driven by a heat-releasing scalar component. *Acta Mechanica Sin.* **38** (10), 321584.
- ELGHOBASHI, S. 1994 On predicting particle-laden turbulent flows. *Appl. Sci. Res.* **52** (4), 309–329.
- FERENC, J. & NÉDA, Z. 2007 On the size distribution of Poisson Voronoï cells. *Phys. A* **385** (2), 518–526.
- FRANKEL, A., POURANSARI, H., COLETTI, F. & MANI, A. 2016 Settling of heated particles in homogeneous turbulence. *J. Fluid Mech.* **792**, 869–893.
- GOLUSKIN, D. & VAN DER POEL, E.P. 2016 Penetrative internally heated convection in two and three dimensions. *J. Fluid Mech.* **791**, R6.
- GROSSMANN, S. & LOHSE, D. 2000 Scaling in thermal convection: a unifying theory. *J. Fluid Mech.* **407**, 27–56.
- GROSSMANN, S. & LOHSE, D. 2001 Thermal convection for large Prandtl numbers. *Phys. Rev. Lett.* **86** (15), 3316–3319.
- GROSSMANN, S. & LOHSE, D. 2002 Prandtl and Rayleigh number dependence of the Reynolds number in turbulent thermal convection. *Phys. Rev. E* **66** (1 Pt 2), 016305.
- GROSSMANN, S. & LOHSE, D. 2004 Fluctuations in turbulent Rayleigh–Bénard convection: the role of plumes. *Phys. Fluids* **16** (12), 4462–4472.
- IRELAND, P.J., BRAGG, A.D. & COLLINS, L.R. 2016 The effect of Reynolds number on inertial particle dynamics in isotropic turbulence. Part 1. Simulations without gravitational effects. *J. Fluid Mech.* **796**, 617–658.
- JIANG, K., DU, X., KONG, Y., XU, C. & JU, X. 2019 A comprehensive review on solid particle receivers of concentrated solar power. *Renew. Sustain. Energy Rev.* **116**, 109463.
- KAZEMI, S., OSTILLA-MÓNICO, R. & GOLUSKIN, D. 2022 Transition between boundary-limited scaling and mixing-length scaling of turbulent transport in internally heated convection. *Phys. Rev. Lett.* **129**, 024501.
- KUERTEN, J.G.M., VAN DER GELD, C.W.M. & GEURTS, B.J. 2011 Turbulence modification and heat transfer enhancement by inertial particles in turbulent channel flow. *Phys. Fluids* **23** (12), 123301.
- LEPOT, S., AUMAÎTRE, S. & GALLET, B. 2018 Radiative heating achieves the ultimate regime of thermal convection. *Proc. Natl Acad. Sci. USA* **115** (36), 8937–8941.
- MONCHAUX, R., BOURGOIN, M. & CARTELLIER, A. 2010 Preferential concentration of heavy particles: a Voronoï analysis. *Phys. Fluids* **22** (10), 103304.
- ORESTA, P. & PROSPERETTI, A. 2013 Effects of particle settling on Rayleigh–Bénard convection. *Phys. Rev. E* **87** (6), 063014.
- OSTILLA-MONICO, R., YANG, Y., VAN DER POEL, E.P., LOHSE, D. & VERZICCO, R. 2015 A multiple-resolution strategy for direct numerical simulation of scalar turbulence. *J. Comput. Phys.* **301**, 308–321.
- PAN, M., DONG, Y., ZHOU, Q. & SHEN, L. 2022 Flow modulation and heat transport of radiatively heated particles settling in Rayleigh–Bénard convection. *Comput. Fluids* **241**, 105454.
- PARK, H.J., O’KEEFE, K. & RICHTER, D.H. 2018 Rayleigh–Bénard turbulence modified by two-way coupled inertial, nonisothermal particles. *Phys. Rev. Fluids* **3** (3), 034307.
- POURANSARI, H. & MANI, A. 2017 Effects of preferential concentration on heat transfer in particle-based solar receivers. *J. Sol. Energy Engng* **139** (2), 021008.
- ROBERTS, P.H. 1967 Convection in horizontal layers with internal heat generation. Theory. *J. Fluid Mech.* **30** (1), 33–49.
- SARDINA, G., SCHLATTER, P., BRANDT, L., PICANO, F. & CASCIOLA, C.M. 2012 Wall accumulation and spatial localization in particle-laden wall flows. *J. Fluid Mech.* **699**, 50–78.
- SHAW, R.A. 2003 Particle-turbulence interactions in atmospheric clouds. *Annu. Rev. Fluid Mech.* **35** (1), 183–227.
- SHOTORBAN, B., MASHAYEK, F. & PANDYA, R.V.R. 2003 Temperature statistics in particle-laden turbulent homogeneous shear flow. *Intl J. Multiphase Flow* **29** (8), 1333–1353.

*Wall-bounded turbulent driven by heat-releasing particle*

- SHRAIMAN, B.I. & SIGGIA, E.D. 1990 Heat transport in high-Rayleigh-number convection. *Phys. Rev. A* **42**, 3650–3653.
- SUN, C., CHEUNG, Y.H. & XIA, K.-Q. 2008 Experimental studies of the viscous boundary layer properties in turbulent Rayleigh–Bénard convection. *J. Fluid Mech.* **605**, 79–113.
- VAN HEERDEN, C., NOBEL, A.P.P. & VAN KREVELEN, D.W. 1953 Mechanism of heat transfer in fluidized beds. *Ind. Engng Chem.* **45** (6), 1237–1242.
- VERZICCO, R. & ORLANDI, P. 1996 A finite-difference scheme for three-dimensional incompressible flows in cylindrical coordinates. *J. Comput. Phys.* **123** (2), 402–414.
- WANG, Q., LOHSE, D. & SHISHKINA, O. 2020 Scaling in internally heated convection: a unifying theory. *Geophys. Res. Lett.* **48**, e2020GL091198.
- YANG, W., ZHANG, Y.-Z., WANG, B.-F., DONG, Y. & ZHOU, Q. 2021 Dynamic coupling between carrier and dispersed phases in Rayleigh–Bénard convection laden with inertial isothermal particles. *J. Fluid Mech.* **930**, A24.
- ZAMANSKY, R., COLETTI, F., MASSOT, M. & MANI, A. 2014 Radiation induces turbulence in particle-laden fluids. *Phys. Fluids* **26** (7), 071701.
- ZAMANSKY, R., COLETTI, F., MASSOT, M. & MANI, A. 2016 Turbulent thermal convection driven by heated inertial particles. *J. Fluid Mech.* **809**, 390–437.